Modeling the effect of anisotropy of gas diffusion layer on transport phenomena in a direct methanol fuel cell

Zheng Miao, Ya-Ling He*, Jin-Qiang Zou

State Key Laboratory of Multiphase Flow in Power Engineering, School of Energy and Power Engineering, Xi'an Jiaotong University, Xi'an, Shaanxi 710049, China

ABSTRACT

Transport phenomena in the gas diffusion layer (GDL) are of vital importance for the operation of direct methanol fuel cells (DMFCs). In this work, a two-phase mass transport model is developed to investigate the effects of anisotropic characteristics of a GDL, including the inherent anisotropy, deformation, and electrical and thermal contact resistances, on the coupled species, charges and thermal transport processes in a DMFC. In this model, methanol crossover and non-equilibrium evaporation/condensation of water and methanol are considered. The multistep electrochemical mechanisms are used to obtain a detailed description of the kinetics of methanol oxidization reaction (MOR) in both the anode and cathode catalyst layers (CLs). The numerical results show that the anisotropy of the GDL has a great effect on the distribution of species concentration, overpotential, local current density, and temperature. The deformation of the GDL depresses the transport of species through the GDL, particularly methanol diffusion in anode GDL, but facilitates the transport of electron and the removal of heat. The electrical contact resistance plays an important role in determining the cell performance.

© 2009 Elsevier B.V. All rights reserved.

1. Introduction

Direct methanol fuel cell is regarded as one of the most promising alternative power sources for portable devices [1]. It has received more and more attentions because it is believed that the DMFC will gain significant market in the future. As the performance improvement is still required for wide application [2], it is essential to get a better understanding of local transport phenomena occurring in components of the DMFC.

GDLs are key components in DMFCs and have a great effect on the cell performance. GDLs are typically made of highly porous carbon cloth or carbon paper. These structures fulfill the functions of passage for reactants and products, electronic conductivity, heat removal and mechanical support for the MEA. This feature of carbon cloth and carbon paper makes the GDLs exhibit strong anisotropic transport properties. In addition to this inherent anisotropy, the shape deformation of GDLs under inhomogeneous compression of the float plate (FP) will also change the transport properties. This is defined as the deformation induced anisotropy in this paper. As DMFC has several layers of components assembly together, the thermal and electrical contact resistance at the Rib/GDL and GDL/CL interfaces will hinder the transport of electron and heat. The contact resistances are related to materials and surface conditions of

the adjacent components, and are also influenced by the inhomogeneous compression on the GDL, so they are also treated as one aspect of the anisotropic factors in this paper.

Up to now, many models considering anisotropic effects of GDLs have been developed. Only a few of them considered the shape deformation effect and contact resistances. Effects of the anisotropic electrical resistance of the GDL in a PEM fuel cell on the current distribution and cell performance are numerically investigated by Zhou and Liu [3]. From their results, it was found that when realistic values of electrical resistance are used, there is no significant change in the characteristics of current distribution in the region under the rib and channel. Ge [4], from the same research group, experimentally tested the effect of compression on the GDL on the performance of PEMFC. And the experimental results show that the amount of compression has a significant influence on the cell performance. Pharoah et al. [5,6] investigated the anisotropic effects of mass diffusivity, electronic conductivity, thermal conductivity, and hydraulic permeability in the PEM fuel cell. It was demonstrated by the results that the isotropic and anisotropic models yield mostly identical polarization curves, however, the current density distributions are completely different. Himanen et al. [7–12] did a series of work on investigating the effect of inhomogeneous compression of PEM fuel cell gas diffusion layer through both experimental tests and numerical methods. Deformation affected physical properties, including the GDL intrusion into the channel, permeability, porosity, in-plane and through-plane bulk electric/thermal conductivities, and electrical

Nomenclature

List of symbols

A	specific area in the catalyst layer ($m^2\,m^{-3}$)
C	concentration ($mol\,m^{-3}$)
D	diffusivity ($m^2\,s^{-1}$)
F	faraday constant (96,485 c mol^{-1})
G	Gibbs free energy ($J\,mol^{-1}$)
h	height of channel or rib (m)
h_V	evaporation heat of water ($J\,mol^{-1}$)
H	enthalpy ($J\,mol^{-1}$)
i	electrochemical reaction rate ($A\,m^{-3}$)
I	current density ($A\,m^{-3}$)
$\mathbf{I}$	current vector ($A\,m^{-3}$)
K	absolute permeability of porous media (m^2)
k_c	condensation rate of water (s^{-1})
k_e	evaporation rate of water ($atm^{-1}\,s^{-1}$)
k_H	henry's law constant
k_{rg}	relative permeability of gas phase
k_{rl}	relative permeability of liquid phase
L	length of the channel (m)
$\dot{m}$	source terms in mass conservation equations ($kg\,m^{-3}\,s^{-1}$)
M	molecular weight ($kg\,mol^{-1}$)
n_d	electro-osmotic drag coefficient
N	molar flux ($mol\,m^2\,s^{-1}$)
p	pressure (pa)
p_c	capillary pressure (pa)
Q	volume flow rate ($ml\,min^{-1}$)
q	switch factor
R	gas constant ($J\,mol^{-1}\,K^{-1}$)
$\dot{R}$	source term in species conservation equations ($mol\,m^{-3}\,s^{-1}$)
R_w	interfacial transfer rate of water ($mol\,m^{-3}\,s^{-1}$)
s	liquid saturation
T	temperature (K)
$\mathbf{u}$	superficial velocity vector ($m\,s^{-1}$)
V_0	thermodynamic equilibrium voltage (V)
V_{cell}	cell voltage (V)

Greek

α	transfer coefficient
γ	reaction order
δ_N	thickness of Nafion coating (m)
ε	porosity of the porous media
κ	thermal conductivity ($W\,m^{-1}\,K^{-1}$)
μ	viscosity ($kg\,m^{-1}\,s^{-1}$)
θ	overlapping angle (°)
θ_c	contact angle (°)
ρ	density ($kg\,m^{-3}$)
σ	interfacial tension ($N\,m^{-1}$)/conductivity ($\Omega^{-1}\,m^{-1}$)

Superscripts

channel	the flow channel
eff	effective value
in	inlet of the flow channel
ref	reference value
sat	saturated

Subscripts

a	anode
acl	anode catalyst layer
adl	anode diffusion layer
c	cathode

ccl	cathode catalyst layer
cdl	cathode diffusion layer
e^-	electrons
H^+	protons
mem	membrane
g	gas phase
l	liquid phase
m	the membrane phase
N	Nafion phase
O_2	oxygen
s	the solid phase
WV	water vapor
MV	methanol vapor

and thermal contact resistances are tested by experiments. Then, the coefficients obtained from their experimental results were used in the numerical models to evaluate the effects of both inherent anisotropy and deformation on cell performance and on local transport phenomena, such as local current density distribution and temperature distribution. However, their numerical models are limited in the single-phase model and the effect of anisotropy on species diffusion coefficients were not considered. The effect of deformation of GDL on the performance of PEM fuel cells has also been numerically studied by Zhou et al. [13,14]. Change of porosity and contact resistance caused by deformation were considered in their model. However, the effects of inherent anisotropy and the electrical resistance were not taken into account. A simplified isotropic numerical treatment for solving the anisotropic electron transport phenomenon in PEM fuel cells was proposed by Meng [15]. Pasaogullari et al. [16] presented a non-isothermal two-phase model for the cathode of PEM fuel cells to investigate the coupled heat and water transport in the cathode GDL. They have found that the inherent anisotropy has a great effect on the temperature distribution and the transport of water. Similar work was done by Ju [17] and the results show that the spatial variation of GDL/CL contact resistance has a strong impact on thermal and two-phase transport characteristics in a PEM fuel cell. A numerical investigation of the coupled electrical conduction and mass diffusion in the cathode GDL of a PEM fuel cell was performed by Sui and Djilali [18] using a simplified 2D simulation. Their results show that "the current density distribution under the land area can be dominated by either electron transport or mass transport, depending on the operating regime". More recently, a 2D two-phase isothermal model was developed by Yang et al. [19] to investigate the coupled electron and two-phase mass transport in the cathode of a PEM fuel cell. Both the effects of the inherent anisotropy and deformation of the GDL were taken into account.

From the review of the literatures above, it can be concluded that transport processes, including mass transport, charges transport, and heat transport are coupled together. These processes should be investigated carefully by a sound mathematical model involving the important anisotropic factors, such as inherent anisotropy, the deformation and the electrical and thermal contact resistances. In additionally, all the numerical models above are developed for the PEMFC. The transport processes in the DMFC are also complicated and the anisotropic effects of the GDL need to be investigated. However, few anisotropic models for DMFCs can be found in the open published literatures. More recently, Most et al. [20] presented an analysis of the diffusive mass transport in the anode side porous backing layer of a direct methanol fuel cell. In their work, the effective transport coefficients of methanol for different backing layers at various compressions were measured. And the Monte Carlo simulation was conducted to calculate the limiting current densities

for a DMFC with anisotropic and inhomogeneous backing layer properties taken into account.

The purpose of this work is to develop a two-phase anisotropic model for the DMFC. The inherent and deformation induced anisotropy of the GDL, and the electrical and thermal contact resistances on the Rib/GDL and the GDL/CL interfaces are considered. The physical fields related to mass and thermal transport processes, such as distribution of species concentration, velocities, overpotential, local current densities, and temperature are numerically studied. An analysis of the sensitivity of the anisotropic parameters are also conducted.

2. Mathematical model

For the modeling of the anisotropic effects in the PEM fuel cell, only the cathode side should be considered because of the sufficiently large diffusion coefficient of hydrogen. However, in this DMFC model, both the anode and cathode electrodes are involved in the computational domains, considering the low transfer rate of methanol in the anode GDL. Fig. 1 shows a two-dimensional periodic unit of a DMFC, which consists of anode flow channel (FC), anode DL, anode CL, polymer electrolyte membrane (PEM), cathode CL, cathode DL and cathode FC. The boundaries of the modeled geometry are marked by the Arabic numerals.

The governing equations corresponding to this model are given as follows.

2.1. Potential

The PEM is a vital nexus between anode and cathode electrodes as it functions to transport protons and prevent the direct mixing of fuel and the oxidant. The transport of protons in the electrolyte

Fig. 1. Computational domain: (a) geometry of the GDL without deformation and (b) geometry of the deformed GDL.

phase and electrons in the solid phase can be described by

$$\frac{\partial}{\partial x}\left(\sigma_{m,x}\frac{\partial \varphi_m}{\partial x}\right) + \frac{\partial}{\partial y}\left(\sigma_{m,y}\frac{\partial \varphi_m}{\partial y}\right) = i_m \tag{1}$$

$$\frac{\partial}{\partial x}\left(\sigma_{s,x}\frac{\partial \varphi_s}{\partial x}\right) + \frac{\partial}{\partial y}\left(\sigma_{s,y}\frac{\partial \varphi_s}{\partial y}\right) = i_s \tag{2}$$

where σ_m and σ_s are conductivities of electrolyte and solid phases, respectively.

2.2. Species concentration

On the anode side, methanol is supplied in the anode FC, transfers through the anode DL to anode CL. Part of the methanol is oxidized in the anode CL to form carbon dioxide, protons and electrons while the remainder crosses over the PEM to the cathode CL and is totally oxidized there. Oxygen is supplied as oxidant in the cathode FC, and combined with protons and electrons in the cathode CL. The governing equations of methanol transport in the liquid phase can be given as

$$\frac{\partial}{\partial x}(u_l C_M) + \frac{\partial}{\partial y}(v_l C_M) = \frac{\partial}{\partial x}\left(D^{eff}_{M,x}\frac{\partial C_M}{\partial x}\right) + \frac{\partial}{\partial y}\left(D^{eff}_{M,y}\frac{\partial C_M}{\partial y}\right) + \dot{R}_M \tag{3}$$

The mass transport of species in the gas phase are governed by

$$\frac{\partial}{\partial x}(u_g C_{i,g}) + \frac{\partial}{\partial y}(v_g C_{i,g}) = \frac{\partial}{\partial x}\left(D^{eff}_{i,x}\frac{\partial C_{i,g}}{\partial x}\right) + \frac{\partial}{\partial y}\left(D^{eff}_{i,y}\frac{\partial C_{i,g}}{\partial y}\right) + \dot{R}_{i,g} \tag{4}$$

where i denotes the oxygen, water vapor and methanol vapor in the gas phase. The interfacial mass transfer rates of water and methanol between liquid and vapor phases are calculated by expressions as follows [21,22]:

$$\tilde{R}_W = \begin{cases} k_e \dfrac{\varepsilon s \rho_l}{M_W}(p^{sat}_W - y_{WV}p_g), & p^{sat}_W \geq y_{WV}p_g \\[2mm] k_c \dfrac{\varepsilon(1-s)y_{WV}}{RT}(p^{sat}_W - y_{WV}p_g), & p^{sat}_W < y_{WV}p_g \end{cases} \tag{5}$$

$$\tilde{R}_M = A_{lg}h_{lg}s(1-s)\frac{p^{sat}_{MV} - p_{MV}}{RT} \tag{6}$$

where p^{sat}_W and p^{sat}_{MV} denote the saturation pressure of water vapor and methanol vapor.

The liquid and gas velocities in Eqs. (3) and (4) are calculated by the modified Darcy's law:

$$\boldsymbol{u}_l = -\left(\frac{K_x k_{rl}}{\mu_l}\frac{\partial p_l}{\partial x} - \frac{n_d M}{\rho_l}\frac{I_x}{F}\right)\vec{e}_x - \left(\frac{K_y k_{rl}}{\mu_l}\frac{\partial p_l}{\partial y} - \frac{n_d M}{\rho_l}\frac{I_y}{F}\right)\vec{e}_y \tag{7}$$

$$\boldsymbol{u}_g = -\frac{K_x k_{rg}}{\mu_g}\frac{\partial p_g}{\partial x}\vec{e}_x - \frac{K_y k_{rg}}{\mu_g}\frac{\partial p_g}{\partial y}\vec{e}_y \tag{8}$$

if the liquid and gas pressure fields are available. In the expression of liquid velocity, it is noted that the contribution of electro-osmotic drag force to the liquid velocity is considered. The governing equations of the pressures of liquid and gas phases can be given as:

$$\frac{\partial}{\partial x}\left(-\frac{K_x \rho_g k_{rg}}{\mu_g}\frac{\partial p_g}{\partial x}\right) + \frac{\partial}{\partial y}\left(-\frac{K_y \rho_g k_{rg}}{\mu_g}\frac{\partial p_g}{\partial y}\right) = \dot{m}_g \tag{9}$$

$$\frac{\partial}{\partial x}\left(-\frac{K_x \rho_l k_{rl}}{\mu_l}\frac{\partial p_l}{\partial x}\right) + \frac{\partial}{\partial y}\left(-\frac{K_y \rho_l k_{rl}}{\mu_l}\frac{\partial p_l}{\partial y}\right) = \dot{m}_l - \frac{n_d M_W}{F}i_m \tag{10}$$
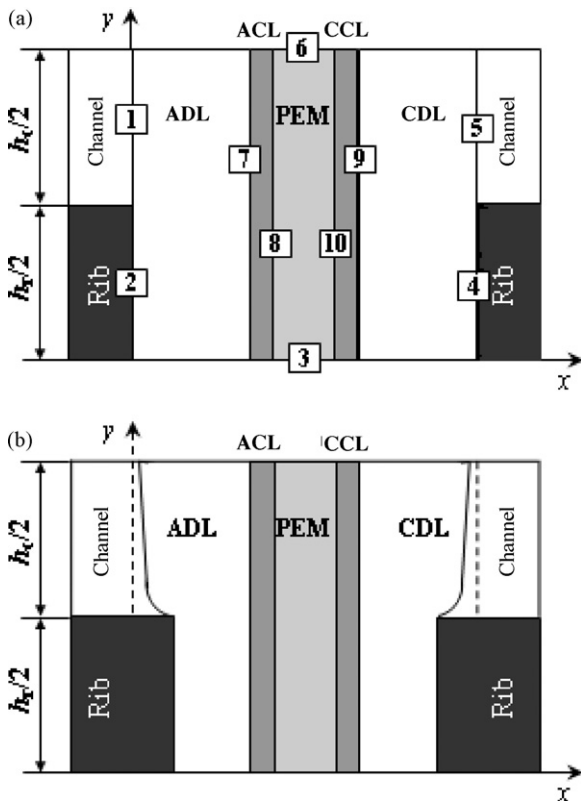
In the anisotropic anode and cathode GDLs, the effective diffusion coefficient of a certain species is calculated by [23–25]

$$D_i^{\text{eff}} = D_i^0 \varepsilon \left(\frac{\varepsilon - \varepsilon_0}{1 - \varepsilon_0} \right)^\alpha (1 - s)^{1.5} \tag{11}$$

where the constant α is 0.521 and 0.785 for in-plane and through-plane diffusions, respectively. In the CLs, the effective diffusion coefficient is

$$D_i^{\text{eff}} = D_i^0 \varepsilon^{1.5} (1 - s)^{1.5} \tag{12}$$

The liquid saturation in Eqs. (10) and (11) is obtained by solving the saturation governing equations below:

ADL, ACL:

$$\frac{\partial}{\partial x} \left(\frac{K_x \rho_l k_{rl}}{\mu_l} \right) \left(\frac{dp_c}{ds} \right) \frac{\partial s}{\partial x} + \frac{\partial}{\partial y} \left(\frac{K_y \rho_l k_{rl}}{\mu_l} \right) \left(\frac{dp_c}{ds} \right) \frac{\partial s}{\partial y}$$

$$= \dot{m}_l + \frac{n_d M_W}{F} i_m - \frac{\rho_l k_{rl} \mu_g}{\rho_g k_{rg} \mu_l} \dot{m}_g \tag{13}$$

CDL, CCL:

$$\frac{\partial}{\partial x} \left(\frac{K_x \rho_g k_{rg}}{\mu_g} \right) \left(\frac{dp_c}{ds} \right) \frac{\partial s}{\partial x} + \frac{\partial}{\partial y} \left(\frac{K_y \rho_g k_{rg}}{\mu_g} \right) \left(\frac{dp_c}{ds} \right) \frac{\partial s}{\partial y}$$

$$= \dot{m}_g - \frac{\rho_g k_{rg} \mu_l}{\rho_l k_{rl} \mu_g} \left(\dot{m}_l + \frac{n_d M_W}{F} i_m \right) \tag{14}$$

where p_c is the capillary pressure and is expressed as follows:

$$p_c = p_g - p_l = \sigma \cos \theta_c (\varepsilon/K)^{0.5} J(s) \tag{15}$$

$$J(s) = \begin{cases} 1.417(1-s) - 2.12(1-s)^2 + 1.263(1-s)^3 & 0° \le \theta_c < 90° \\ 1.417s - 2.12s^2 + 1.263s^3 & 90° \le \theta_c < 180° \end{cases} \tag{16}$$

2.3. Temperature

Heat transport in the GDL is modeled by the energy conservation equation as follows:

$$\frac{\partial}{\partial x} (\rho_g C_{p,g} u_g T + \rho_l C_{p,l} u_l T) + \frac{\partial}{\partial x} (\rho_g C_{p,g} v_g T + \rho_l C_{p,l} v_l T)$$

$$= \frac{\partial}{\partial x} \left(\kappa_x^{\text{eff}} \frac{\partial T}{\partial x} \right) + \frac{\partial}{\partial y} \left(\kappa_y^{\text{eff}} \frac{\partial T}{\partial y} \right) + \dot{R}_T \tag{17}$$

where the source term $\dot{R}_T$ is the heat generation rate in the DMFC, and contains the irreversible heat release from the electrochemical reactions, reversible entropic heat, Joule heating due to electrical and ionic resistances, and heat source due to the non-equilibrium condensation/evaporation of water and methanol.

2.4. Electrochemical kinetics

In the present model, the multistep mechanism [26,27] is considered for the MOR in the anode CL:

$$CH_3OH \underset{k_1'}{\overset{k_1}{\rightleftharpoons}} CH_3OH_{ads} \tag{18}$$

$$CH_3OH_{ads} \xrightarrow{k_2} CO_{ads} + 4H^+ + 4e^- \tag{19}$$

$$H_2O \underset{k_3'}{\overset{k_3}{\rightleftharpoons}} OH_{ads} + H^+ + e^- \tag{20}$$

Table 1
Kinetics parameters of methanol oxidization reaction.

Parameters	Value		Unit
	Anode	Cathode	
k_1	4.1×10^{-13}	4.0×10^{-12}	ms^{-1}
k_1'	1.54×10^{-10}	1.54×10^{-10}	$mol\,m^{-2}\,s^{-1}$
k_2	3.6×10^{-16}	3.6×10^{-16}	$mol\,m^{-2}\,s^{-1}$
k_3	1.2×10^{-13}	1.2×10^{-13}	$mol\,m^{-2}\,s^{-1}$
k_3'	0.13	1.3	$mol\,m^{-2}\,s^{-1}$
k_4	2.0×10^{-2}	2.0×10^{-2}	$mol\,m^{-2}\,s^{-1}$
α_2	0.79	0.8	
β_3	0.5	0.5	
β_4	0.5	0.5	

$$CO_{ads} + OH_{ads} \xrightarrow{k_4} CO_2 + H^+ + e^- \tag{21}$$

Using Eqs. (18)–(21), one can obtain the surface coverage of species as follows:

$$\theta_{CO} = b \frac{k_2 \exp(\alpha_2 F \eta_M / RT)}{k_4 \exp((1 - \beta_4) F \eta_M / RT)} \tag{22}$$

$$\theta_{OH} = \frac{k_1 \tilde{C}_M (1 - \theta_{CO})}{b[k_1' + k_2 \exp(\alpha_2 F \eta_M / RT) + k_1 \tilde{C}_M] + k_1 \tilde{C}_M} \tag{23}$$

where b is expressed as

$$b = \frac{k_3' \exp(-\beta_3 F \eta_M / RT)}{[k_1' + k_2 \exp(\alpha_2 F \eta_M / RT)]k_3 \exp[(1 - \beta_3) F \eta_M / RT] / ((k_1 \tilde{C}_M) + k_2 \exp(\alpha_2 F \eta_M / RT))} \tag{24}$$

k_i, α_i, and β_i in Eqs. (22)–(24) denote rate constants, transfer coefficients and symmetry factors of respective reactions.

This multistep mechanism is also used for the direct methanol oxidization reaction (DMOR) in the cathode CL by modifying some kinetic parameters, listed in Table 1. $\tilde{C}_M$ in Eqs. (23) and (24) is the mean concentration of methanol in the CLs, and can be calculated by

$$\tilde{C}_M = s C_M + (1 - s) C_{MV} \tag{25}$$

And η_M is the overpotential in CLs for the oxidization reaction of methanol.

$$\eta_M = \begin{cases} \varphi_{s,a} - \varphi_{m,a} & \text{anode} \\ \varphi_{s,c} - \varphi_{m,c} & \text{cathode} \end{cases} \tag{26}$$

Finally, the MOR rate in anode CL i_a and DMOR rate in cathode CL i_p can be given in a identical form:

$$i_M = 6aFKk_4 \exp \left(\frac{(1 - \beta_4) F \eta_M}{RT} \right) \theta_{CO} \theta_{OH} \tag{27}$$

where K is the proportionality constant.

Kinetics of oxygen reaction rate (ORR) in the cathode CL is calculated by

$$i_c = (1 - s) A_c i_{O_2}^{\text{ref}} \left(\frac{C_{O_2}}{C_{O_2}^{\text{ref}}} \right) \exp \left[\frac{\alpha_c F}{RT} \eta_c \right] \xi_{O_2} \tag{28}$$
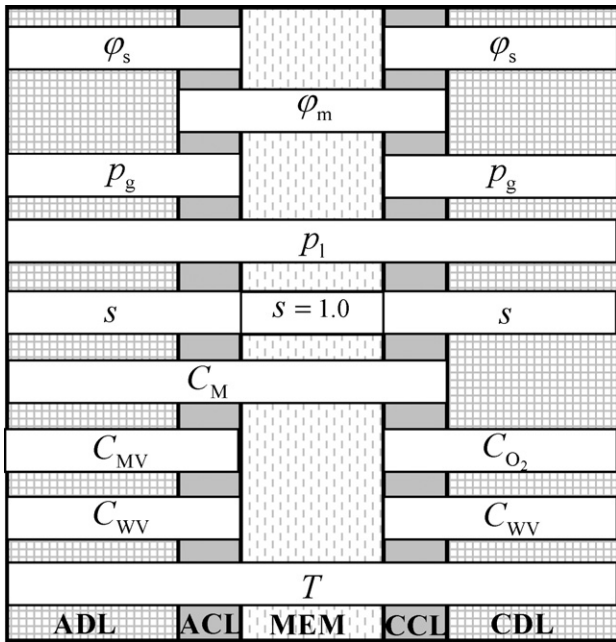
Fig. 2. Specified computational sub-domains for the solving variables.

ξ_{O_2} in Eq. (28) is the correction factor derived from the modified agglomerate model [28], and denotes the effect of the transfer resistance in the Nafion coating and the agglomerate.

2.5. Current balance and cell voltage

In a working fuel cell, the mean current densities at the anode and cathode electrodes can be calculated by

$$I_a = \frac{\iint_{ACL} i_a \, dx \, dy}{h_c + h_r} \tag{30}$$

$$I_c = \frac{\iint_{CCL} i_c \, dx \, dy}{h_c + h_r} \tag{31}$$

$$I_p = \frac{\iint_{CCL} i_p \, dx \, dy}{h_c + h_r} \tag{32}$$

Because part of oxygen is consumed by the DMOR in the cathode CL, the current conservation equation can be expressed as

$$I_{cell} = I_a = I_c - I_p \tag{33}$$

where the 'parasitic' current, I_p, is a virtual current density and denotes the fuel loss caused by methanol crossover.

Finally, the cell voltage can be determined from the expression as follows:

$$V_{cell} = \varphi_{s,c}^0 \tag{34}$$

where $\varphi_{s,c}^0$ is the solid phase potential of the cathode ribs.

Up to this point, all the governing equations related to the two-phase mass transport and electrochemical reactions have been presented. In order to exhibit the detailed information of the

where η_c is the overpotential for ORR in the cathode CL, and can be expressed as

$$\eta_c = V_0 + \varphi_{m,c} - \varphi_{s,c} \tag{29}$$

Table 2
Expressions of source terms and coefficients of the governing equations.

Parameters	Expressions
Generation rate of charges	$i_m = \begin{cases} i_a & ACL \\ i_c - i_p & CCL \\ 0 & MEM \end{cases}$, $i_s = \begin{cases} -i_a & ACL \\ i_p - i_c & CCL \\ 0 & GDLs \end{cases}$
Mole generation rate of species	$\dot{R}_M = \begin{cases} -i_a/(6F) & ACL \\ -i_p/(6F) & CCL \\ 0 & ADL, MEM \end{cases}$, $\dot{R}_{O_2} = \begin{cases} -i_c/(4F) & CCL \\ 0 & CDL \end{cases}$, $\dot{R}_{MV} = \begin{cases} \tilde{R}_M & ACL \\ \tilde{R}_M & ADL \end{cases}$, $\dot{R}_{WV} = \begin{cases} \tilde{R}_W & CLs \\ \tilde{R}_W & GDLs \end{cases}$, $\dot{R}_{CO_2} = \begin{cases} i_a/(6F) & ACL \\ i_p/(6F) & CCL \end{cases}$
Generation rate of mass in gas and liquid phase	$\dot{m}_g = \begin{cases} M_W \tilde{R}_W + M_M \tilde{R}_{MV} & ADL \\ M_W \tilde{R}_W + M_M \tilde{R}_{MV} + M_{CO_2} \tilde{R}_{CO_2} & ACL \\ M_W \tilde{R}_W - M_{O_2} \tilde{R}_{O_2} + M_{CO_2} \tilde{R}_{CO_2} & CCL \\ M_W \tilde{R}_W & CDL \end{cases}$, $\dot{m}_l = -\dot{m}_g$
Generation rate of heat	$\dot{R}_T = \begin{cases} |I|^2/\sigma_s + h_{v,W}\dot{R}_W + h_{v,M}\dot{R}_M & ADL \\ i_a(\eta_a - (\Delta H_a - \Delta G_a)/6F) + |I|^2/\sigma_s + h_{v,W}\dot{R}_W + h_{v,M}\dot{R}_M & ACL \\ |I|^2/\sigma_m & MEM \\ (i_c - i_p)(\eta_c - (\Delta H_c - \Delta G_c)/4F) - i_p\Delta H/6F + |I|^2/\sigma_s + h_{v,W}\dot{R}_W + h_{v,M}\dot{R}_M & CCL \\ |I|^2/\sigma_s + h_{v,W}\dot{R}_W + h_{v,M}\dot{R}_M & CDL \end{cases}$
Relative permeabilities	$k_{rl} = s^3, \ k_{rg} = (1-s)^3$
Thickness of the GDL under inhomogeneous compression	$L(y) = \begin{cases} L_{comp} = 2.5 \times 10^{-4} \text{ m} & \text{under-rib} \\ 19.30314 \log((y - 0.0005) \times 10^6 + 1) \times 10^{-6} + L_{comp} & \text{under-channel} \end{cases}$
Porosity of the GDL under inhomogeneous compression	$\varepsilon(y) = \varepsilon_0(L(y) - L_{min})/L_0 - L_{min}, \ L_{min} = L_0 \times (1 - \varepsilon_0)$
In-plane permeability	$K_{in-p} = 2.754(y^3) - 1.484 \times 10^{-3}L(y)^2 + 2.76 \times 10^{-7}L(y) - 1.7 \times 10^{-11}$
Electrical conductivity of the GDL	$\sigma_{in-p} = -1.159 \times 10^7 L(y) + 6.896 \times 10^3, \ \sigma_{th-p} = -8.385 \times 10^6 L(y) + 3.285 \times 10^3$
Interfacial electrical contact resistance	$r_{e,GDL/CL} = 5.83 \times 10^{-10} \exp(2.06 \times 10^4 L(y)), \ r_{e,Rib,GDL} = 1. \times 10^{-9}(7.726 \times 10^{11}L(y)^3 - 4.943 \times 10^8 L(y)^2 + 2.664 \times 10^4 L(y) + 18.911)^{-1}$
Interfacial thermal contact resistance	$r_{T,Rib/GDL} = 1. \times 10^{-9} \begin{pmatrix} -2.912 \times 10^{14}L(y)^4 + 3.133 \times 10^{11}L(y)^3 \\ -1.17 \times 10^8 L(y)^2 + 1.639 \times 10^4 L(y) - 0.438 \end{pmatrix}^{-1}, \ r_{T,GDL/CL} = r_{T,Rib/GDL}$

Table 3
Cell geometric dimensions and base case of the model.

Parameters	Symbols	Value	Unit
Structure parameters			
Porosity, thickness			
GDL	$\varepsilon_{GDL}, l_{GDL}$	$0.7, 3.8 \times 10^{-4}$	–, m
CL	ε_{CL}, l_{CL}	$0.3, 0.2 \times 10^{-4}$	–, m
MEM	$\varepsilon_{mem}, l_{mem}$	$0.3, 1.3 \times 10^{-4}$	–, m
Height of a half rib	h_r	0.5×10^{-3}	m
Height of a half channel	h_c	0.5×10^{-3}	m
Length of channels	L_c	3×10^{-2}	m
Operation conditions			
Operation temperature	T	333.15	K
Anode channel inlet pressure	$p_{l,a}^{in}$	101,325	pa
Cathode channel inlet pressure	$p_{g,c}^{in}$	101,325	pa
Anode flow rate	$Q_{a,in}$	1	ml min^{-1}
Inlet methanol concentration at anode	C_M^{in}	1000	mol m^{-3}
Inlet oxygen concentration at cathode	$C_{O_2}^{in}$	7.68	mol m^{-3}

governing equations, the computational sub-domains for solving variables are shown in Fig. 2. The expressions of source terms of the specific equations and correlations of several coefficients are listed in Table 2. It is noted that the parameters and correlations obtained from Himanen et al.'s work [7–12] are adopted in the present simulation because the tested GDL is used in both PEMFC and DMFC operation.

2.6. Boundary conditions

Boundaries for the sub-domains are marked with Arabic numerals in Fig. 1. Conditions at each boundary are given as follows:

(I) *Boundary 1:* This boundary is the interface between the anode GDL and anode FC, which is the inlet of methanol solution and outlet of carbon dioxide. This boundary is impermeable for the electrons and heat flux:

$$p_l = p_{l,a}^{in}, \quad p_g = p_{l,a}^{in} + p_{c,a}^{channel}, \quad s = s_a^{channel}, \quad C_M = C_M^{in},$$

$$C_{WV} = C_{WV}^{sat}, \quad C_{MV} = C_{MV}^{sat}, \quad \frac{\partial \varphi_s}{\partial x} = 0, \quad \frac{\partial T}{\partial x} = 0 \qquad (35)$$

(II) *Boundaries 2:* This boundary is the interface between the anode GDL and ribs of the anode FP. This boundary is impermeable for reactants but permeable for electrons and heat

Table 4
Physicochemical properties and parameters used in simulation.

Parameters	Symbols	Value	Unit	References
Physicochemical properties				
Nafion volume fraction in ACL and CCL	$\varepsilon_{N,acl}, \varepsilon_{N,ccl}$	0.4, 0.4		
Conductivity in membrane phase	σ_m	$7.3e^{[1268(1/298-1/T)]}$	Ω^{-1} m^{-1}	[28]
Conductivity in CLs	σ_{cl}	300	Ω^{-1} m^{-1}	[8]
Permeability				
ADL	K_{th-p}	3.74×10^{-11}	m^2	[8]
CLs	K_{cl}	1×10^{-14}	m^2	[30]
MEM	K_{mem}	5×10^{-18}	m^2	
Viscosity of gas phase	μ_g	2.03×10^{-5}	kg m^{-1} s^{-1}	[31]
Viscosity of liquid phase	μ_l	4.06×10^{-4}	kg m^{-1} s^{-1}	[30]
Electro-osmotic coefficients of water	n_d	2.5		[32]
Diffusivities				
Methanol in liquid water	$D_{M,l}$	$10^{-5.4163-999.778/T}$	m^2 s^{-1}	[33]
Methanol in Nafion	$D_{M,N}$	$4.9 \times 10^{-10} e^{[2436(1/333-1/T)]}$	m^2 s^{-1}	[31]
Oxygen in gas phase	$D_{O_2,g}$	$1.775 \times 10^{-5} (T/273.15)^{1.823}$	m^2 s^{-1}	[33]
Oxygen in Nafion	$D_{O_2,N}$	1.844×10^{-10}	m^2 s^{-1}	[34]
Water vapor in gas	$D_{WV,g}$	$2.56 \times 10^{-5} (T/307.15)^{2.334}$	m^2 s^{-1}	[33]
Methanol vapor in gas	$D_{MV,g}$	$-6.954 \times 10^{-6} + 4.5986 \times 10^{-8} T + 9.4979 \times 10^{-11} T^2$	m^2 s^{-1}	[33]
Interfacial transfer rate constant for methanol	h_{lg}	0.001	m^2 s^{-1}	[22]
Specific interfacial area between liquid and gas	A_{lg}	1×10^5	m^{-1}	[22]
Henry law constant for methanol	$k_{H,M}$	$0.096e^{0.04511(T-273)}$	atm	[33]
Henry law constant for oxygen	k_H	$0.3125 \times 101,325/RT$		[35]
Saturation pressure of vapor	$\log_{10} p_W^{sat}$	$-2.1794 + 0.02953(T-273)$ $-9.1837 \times 10^{-5}(T-273)^2$ $+1.4454 \times 10^{-7}(T-273)^3$	atm	[30]
Evaporation rate constant of water	k_e	5×10^{-3}	atm^{-1} s^{-1}	[21]
Condensation rate constant of water	k_c	50	s^{-1}	[21]
Mole enthalpy change of the anode semi-reaction	ΔH_a	126.69	kJ mol^{-1}	
Mole enthalpy change of the cathode semi-reaction	ΔH_c	−567.41	kJ mol^{-1}	
Mole enthalpy change of the overall reaction	ΔH	−724.43	kJ mol^{-1}	
Mole Gibbs free energy change of the anode semi-reaction	ΔG_a	9.35	kJ mol^{-1}	
Mole Gibbs free energy change of the cathode semi-reaction	ΔG_c	−474.16	kJ mol^{-1}	
Liquid methanol specific heat capacity	$C_{p,M}$	89.33	J mol^{-1} K^{-1}	
Liquid water specific heat capacity	$C_{p,W}$	75.48	J mol^{-1} K^{-1}	
Oxygen specific heat capacity	C_{p,O_2}	29.43	J mol^{-1} K^{-1}	
Carbon dioxide specific heat capacity	C_{p,CO_2}	37.21	J mol^{-1} K^{-1}	
Water vapor specific heat capacity	$C_{p,WV}$	33.64	J mol^{-1} K^{-1}	
Electrochemical kinetics parameters				
Exchange current density of ORR	$i_{O_2}^{ref}$	$0.04222e^{(73,200\times(1/353-1/T)/R)}$	A m^{-3}	[33]
Reference concentration of oxygen	$C_{O_2}^{ref}$	p_{O_2}/RT	mol m^{-3}	[16]
Transfer coefficient of cathode	α_c	1.0		[16]
Thermodynamic voltage	V_0	1.21	V	[33]

flux:

$$\frac{\partial p_l}{\partial x} = 0, \quad \frac{\partial p_g}{\partial x} = 0, \quad \frac{\partial s}{\partial x} = 0, \quad \frac{\partial C_M}{\partial x} = 0,$$

$$\frac{\partial C_{WV}}{\partial x} = 0, \quad \frac{\partial C_{MV}}{\partial x} = 0, \quad \varphi_s = \varphi_{s,a}^0, \quad T = T_0 \quad (36)$$

(III) *Boundaries 3 and 6:* The symmetrical conditions for all variables are specified at these two boundaries as the computational domain is a periodic unit of the entire cell:

$$\frac{\partial p_l}{\partial y} = 0, \quad \frac{\partial p_g}{\partial y} = 0, \quad \frac{\partial s}{\partial y} = 0, \quad \frac{\partial C_M}{\partial y} = 0, \quad \frac{\partial C_{WV}}{\partial y} = 0,$$

$$\frac{\partial C_{MV}}{\partial y} = 0, \quad \frac{\partial C_{O_2}}{\partial y} = 0, \quad \frac{\partial \varphi_s}{\partial y} = 0, \quad \frac{\partial \varphi_m}{\partial y} = 0, \quad \frac{\partial T}{\partial y} = 0 \quad (37)$$

(IV) *Boundaries 4:* This boundary is the interface between the cathode GDL and ribs. Similar to boundaries 2, the conditions

at this boundary can be given as

$$\frac{\partial p_l}{\partial x} = 0, \quad \frac{\partial p_g}{\partial x} = 0, \quad \frac{\partial s}{\partial x} = 0, \quad \frac{\partial C_{O_2}}{\partial x} = 0,$$

$$\frac{\partial C_{WV}}{\partial x} = 0, \quad \varphi_s = 0, \quad T = T_0 \quad (38)$$

(V) *Boundary 5:* Similar to boundary 1, this boundary represents the inlet of reactants on the cathode side. The following boundary conditions at this interface are specified:

$$p_l = p_{g,c}^{in} - p_c^{channel}, \quad p_g = p_{g,c}^{in}, \quad s = s_c^{channel},$$

$$C_{O_2} = C_{O_2}^{in}, \quad C_{WV} = 0, \quad \frac{\partial \varphi_s}{\partial x} = 0, \quad \frac{\partial T}{\partial x} = 0 \quad (39)$$

(VI) *Boundaries 7 and 9:* As the left and right boundaries of the electrolyte phase region, which are impermeable for protons. Accordingly, the flux of protons is zero at these two boundaries:
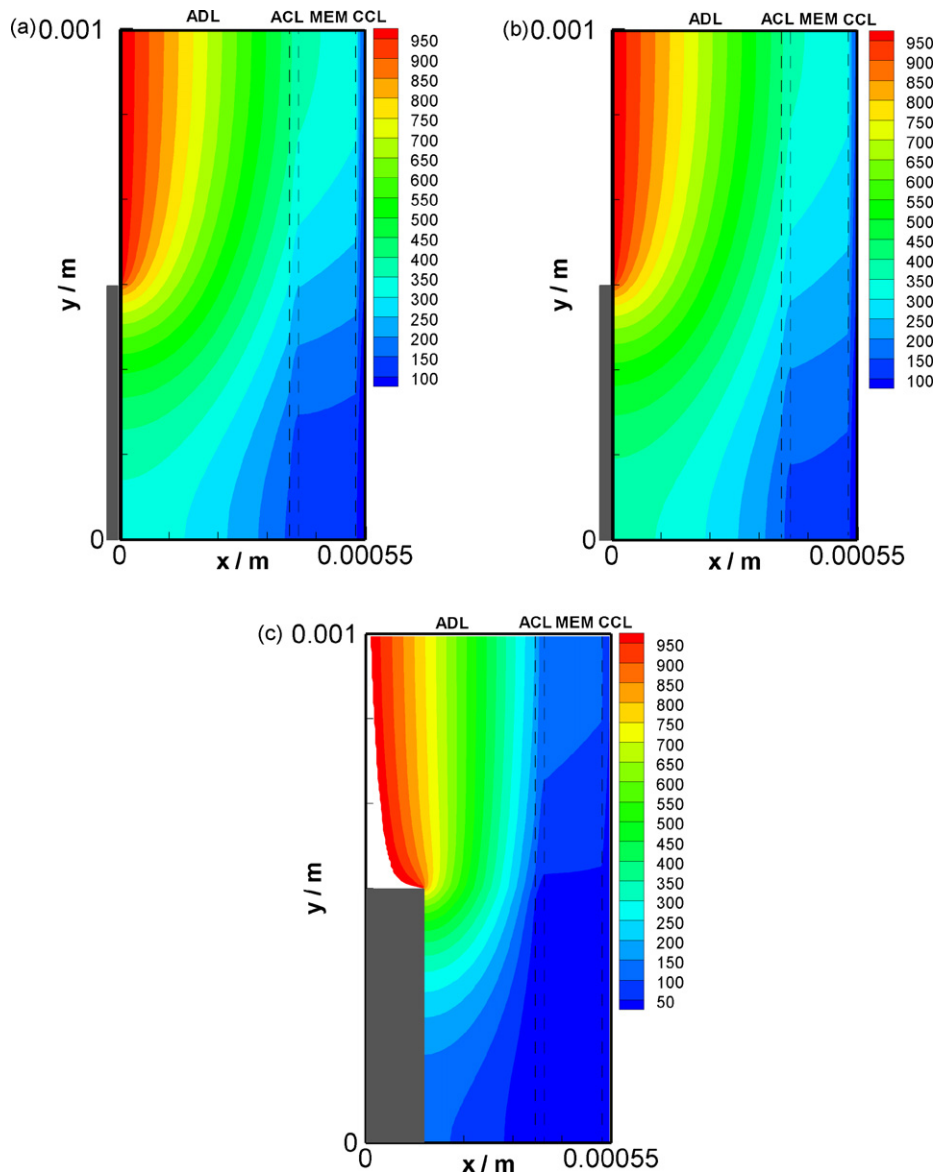
$$N_{H^+} = 0 \quad (40)$$

Fig. 3. Distribution of methanol concentration in anode DL, PEM and CLs.

(VII) *Boundary 8:* This boundary is the interface between the anode CL and PEM. As the membrane is treated as an impermeable wall for the electrons and gas phase, the conditions at this interface can be given as

$$N_{e^-} = 0, \quad N_{WV} = 0, \quad N_{MV} = 0 \tag{41}$$

(VIII) *Boundary 10:* Similar to boundary 8, conditions at this interface can be specified as

$$N_{e^-} = 0, \quad N_{WV} = 0, \quad N_{O_2} = 0 \tag{42}$$

The detailed treatment of pressure and liquid saturation in the flow channel can be referred to our former work [28].

3. Numerical results and discussion

In order to clearly show the effects of the anisotropic properties of the GDL on the transport phenomena, three different cases of GDL were simulated in this work. Isotropic GDL: the GDL is treated as a homogeneous and isotropic porous medium. The through-plane transport coefficients are used for calculation along both through-plane and in-plane directions. Anisotropic GDL: the GDL is homogeneous but anisotropic. Through-plane and in-plane coefficients are adopted for the through-plane and in-plane directions, respectively. Deformed GDL: the GDL is anisotropic porous medium with deformation. The deformation effected through-plane and in-plane coefficients are used.

A self-written computer code based on the finite-volume-method is developed to solve the governing equations iteratively. It is noted that the present model is further developed from our former work [28], in which the mathematical model is verified by experimental data. In the present model, numerical treatments to the GDL geometry and anisotropic transport parameters are employed to capture the anisotropic effects. These treatments have no effect on the mathematic logic of the numerical model. The baseline conditions for this model is listed in Table 3, and parameters and correlations are given in Table 4 [29–35]. The distribution of species concentration, potential, local current density and a sensitive analysis of the anisotropic coefficients are presented below.

3.1. Species and electron transport feature in the electrodes

Distribution of methanol concentration in the anode porous electrode, PEM and cathode CL is presented in Fig. 3(a)–(c). The
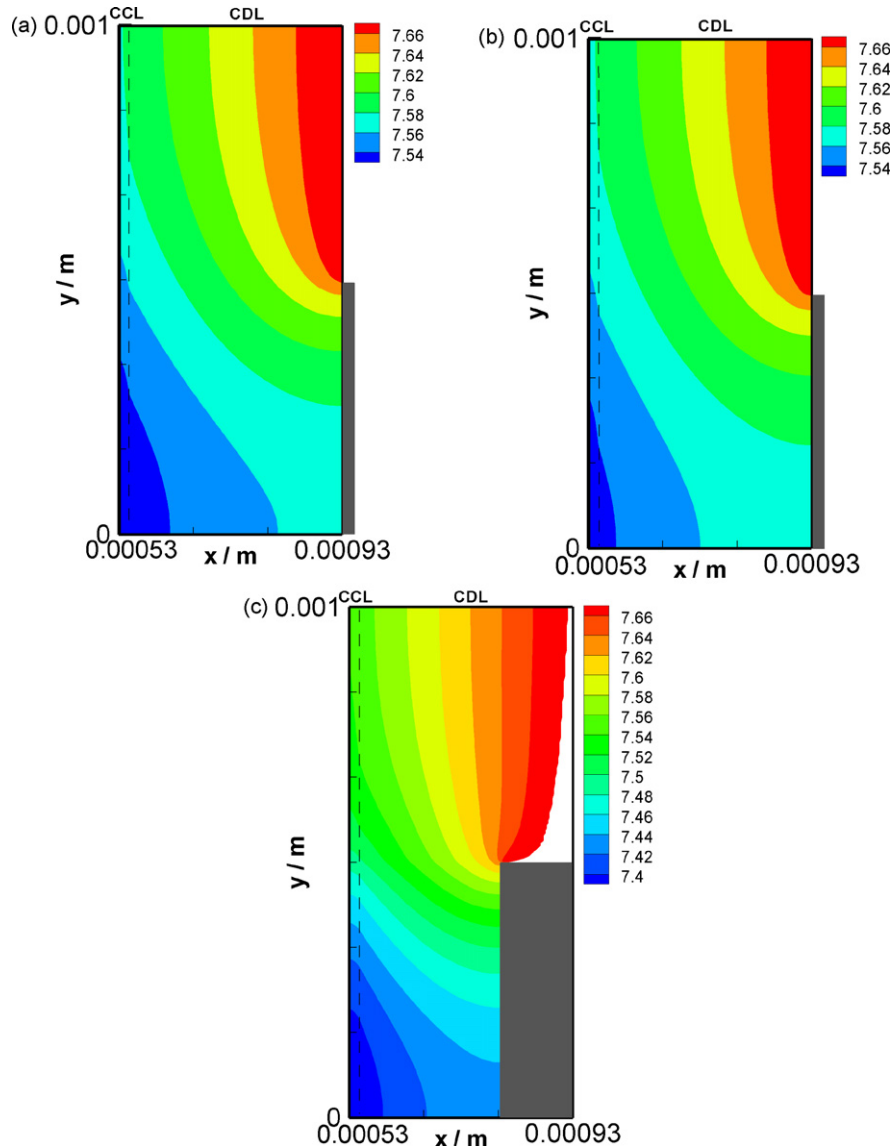

Fig. 4. Distribution of oxygen concentration at the cathode electrode.

inlet methanol concentration is fixed to 1000 mol m^{-3}. It can be seen in Fig. 3(c) that the largest gradient of methanol concentration appears in the deformed GDL. From our former work [28,36], it has been proved that diffusion mechanism dominate the species transport in the DMFC. The inhomogeneous deformation of the GDL leads to a reduction of porosity of the GDL, especially in the region under rib. Consequently, the effective diffusivities of methanol in both in-plane and through-plane directions become much lower. As a result, the methanol concentration in the under-rib region of the deformed GDL gets much smaller. By comparing Fig. 3(a) and (b), it is found that methanol concentration in the region under rib of the anisotropic GDL is relatively higher than that in the isotropic GDL. This is because the in-plane effective diffusivity of methanol for the anisotropic GDL is larger than that for the isotropic GDL. So a relatively smaller gradient of methanol concentration appears in the anisotropic GDL.

The similar trends can be seen in the distribution of oxygen concentration in the cathode electrode in Fig. 4. However, it should be noted that the variation of the oxygen concentration in the GDL is much small because of the high diffusion coefficient of oxygen. Even

in the deformed GDL, the relative ratio of concentration reduction of oxygen is only 3.64%.

The distributions of electrical potential at the anode and cathode electrodes are shown in Figs. 5 and 6. The working current density of DMFCs with these three types of GDL are all keeping at 0.9 A m^{-2}. For the isotropic GDL, the through-plane conductivity of electron is used for calculation on both the in-plane and through-plane directions. It is shown that the largest gradient of electrical potential appears in Figs. 5(a) and 6(a) because of the higher electrical resistance along the in-plane direction. By contrast, the in-plane conductivity in the anisotropic GDL is about 25 times as large as the through-plane conductivity. So in Figs. 5(b) and 6(b), the distribution of electrical potential along the in-plane direction is almost uniform. Electron transport in the GDL exhibits almost one-dimension behavior. These results agree well with results in literatures [16,19]. When the GDL is under inhomogeneous compression, only a much smaller potential gradient is required to drive the electrons to transfer through the GDL, as shown in Figs. 5(c) and 6(c). This is because the contact of fibers in the GDL has a great effect on the transport of electrons. The
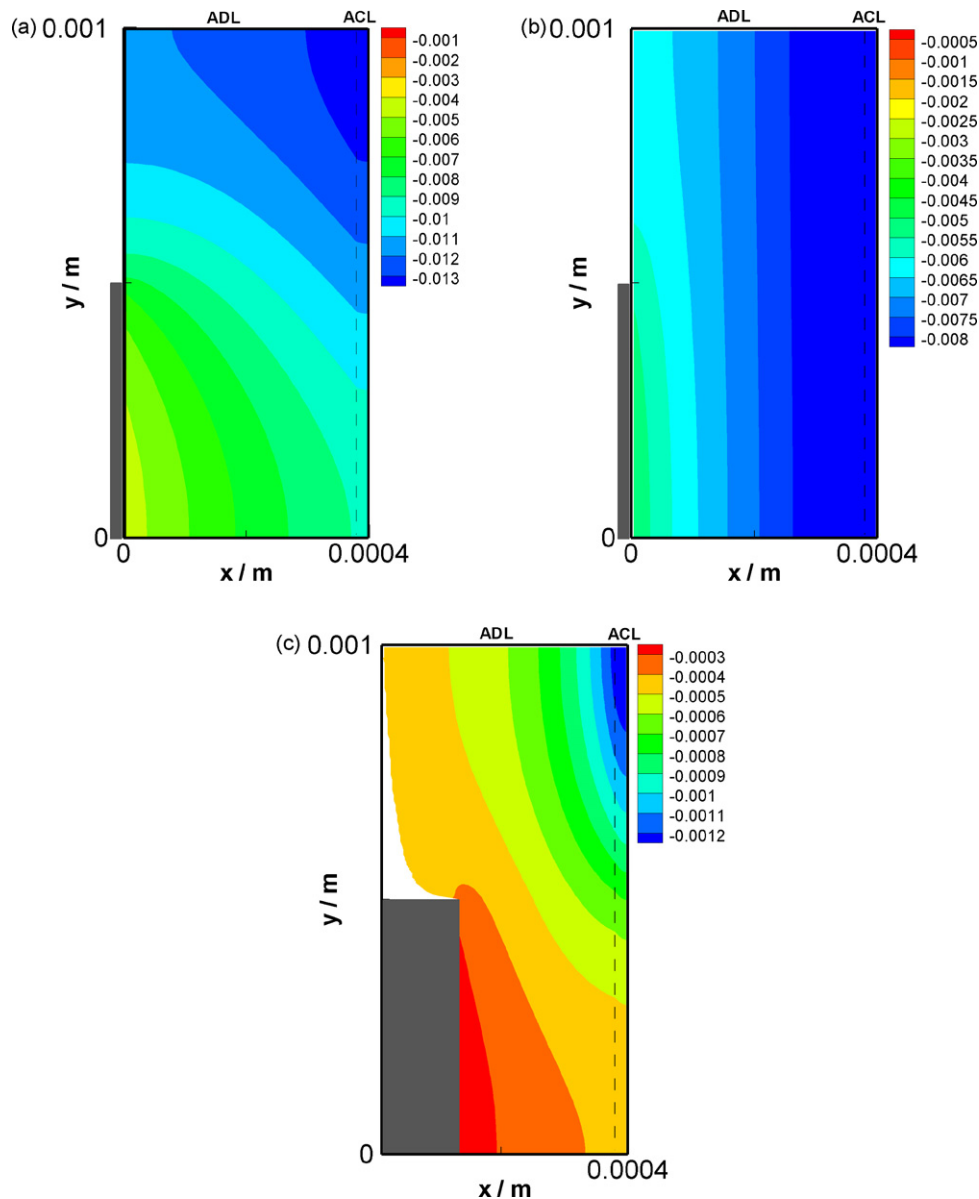

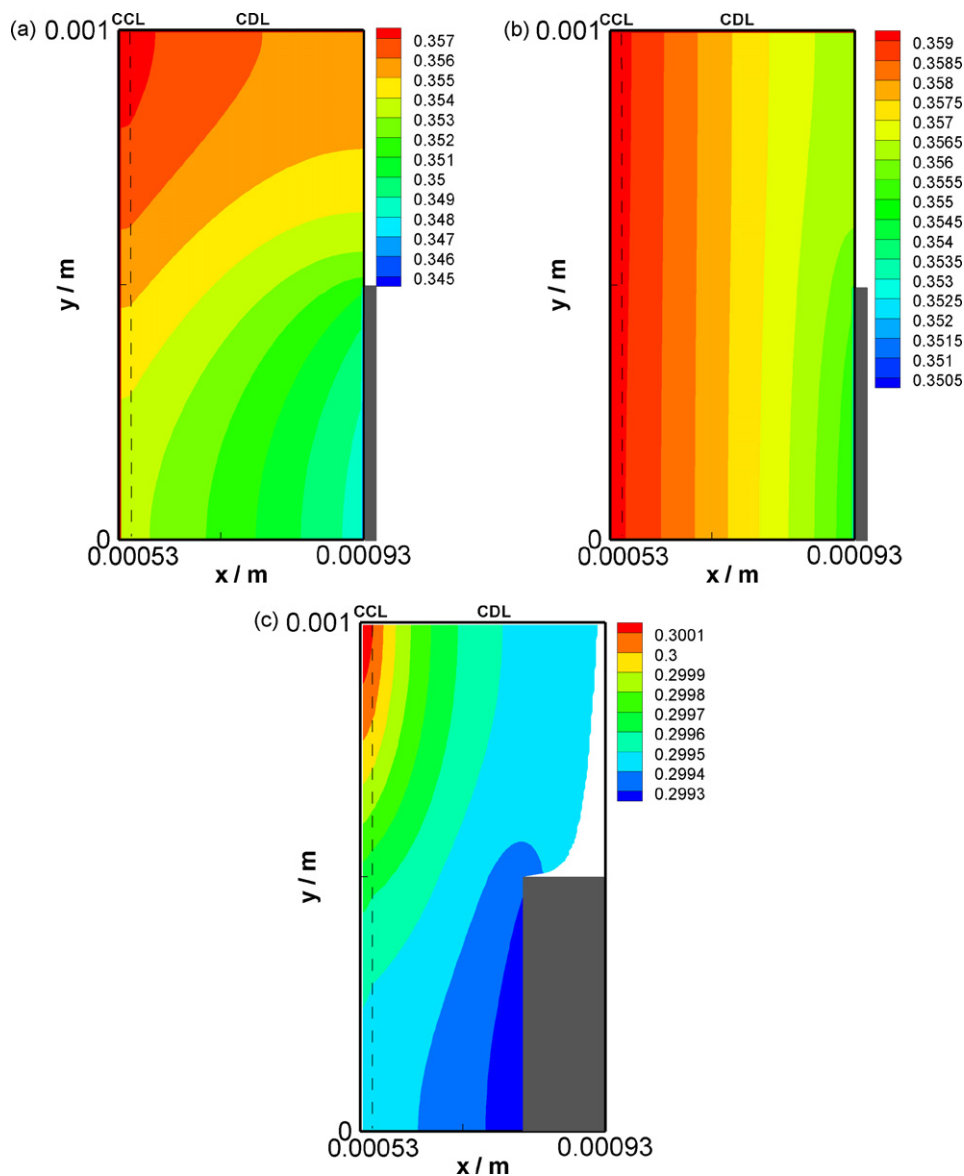Fig. 5. Distribution of electrical potential at the anode electrode.

Fig. 6. Distribution of electrical potential at the cathode electrode.

deformation of the GDL leads to a well contact of the fibers and consequently a significant increase in the electrical conductivity.

3.2. Distribution of key physical fields in the CLs

The distributions of local current density, methanol concentration, overpotential, and the electrical and ionic potential in the anode CL are presented in Fig. 7(a)–(d). It is known that the cell current density results from the combine effects of reactant concentration and overpotential in the CLs. For the anode side, it can be seen in Fig. 7(a)–(c) that the local current density mainly depends on the methanol concentration. The trend of the profile of anode local current density is similar to that of methanol but contrast to that of anode overpotential. A comparison between the cases of isotropic GDL and anisotropic GDL in Fig. 7(a)–(c) shows that the higher in-plane effective diffusivity of methanol promotes the transport of methanol from the region under channel to the region under rib, while the higher conductivity of electron along the in-plane direction for the anisotropic GDL makes it much easier for the electrons to transfer from the rib to the region under channel,

represented by a higher overpotential. Both the higher methanol concentration and higher overpotential can leads to a higher local current density. And as a result of these two aspects, the anode local current density displays two intertwined curves, plotted in Fig. 7(a). This means that the effects of inherent anisotropy of the GDL on methanol transport and on electron transport are limited and comparable. However, Local current density in the anode CL for the case of deformed GDL exhibits a significant non-uniform distribution along the in-plane direction, seen in Fig. 7(a). This is primarily caused by the non-uniform distributed and significantly reduced effective diffusivity of methanol in the GDL under inhomogeneous deformation. So for the case of deformed GDL, most of methanol is consumed in the region under channel. These profiles of anode local current density in Fig. 7(a) are qualitatively in good agreement with the results predicted by the Monte Carlo simulation in Matthias's work [20].

Fig. 8 shows the distributions of local current density, oxygen concentration, overpotential, electrical and ionic potential along the in-plane direction in the cathode CL. Compared with that on the anode side, it can be seen that the local current density in the
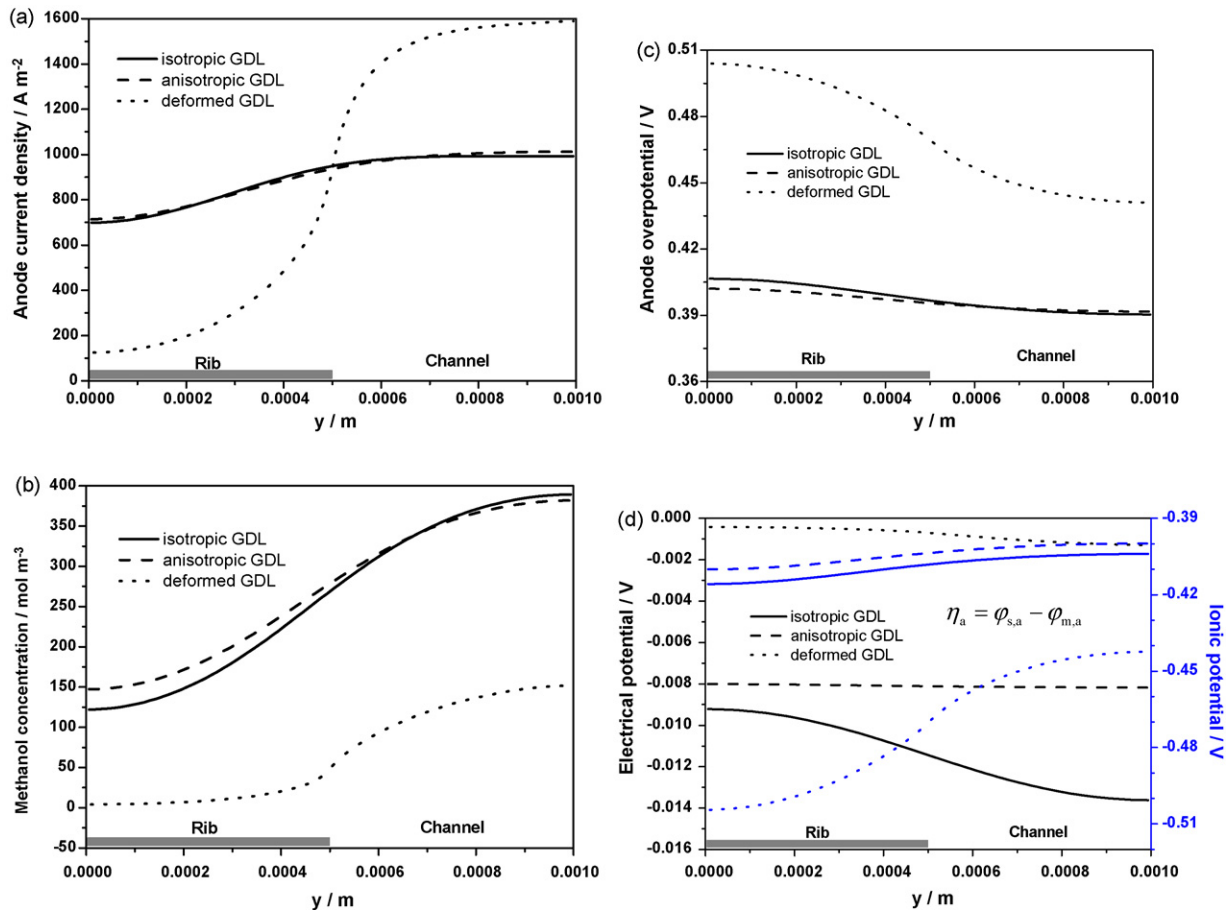
Fig. 7. Distribution of local current density, methanol concentration, anode overpotential, and anode electrical and ionic potential along the in-plane direction in the anode CL.

cathode CL is mainly dominated by the cathode overpotential. This behavior agrees well with our former work [28]. And it is rather different from the phenomenon occurring in the PEMFC [19]. The reason can be concluded in two aspects. In one aspect, the variation of oxygen concentration in the CL of a DMFC is much smaller than that in a PEMFC because of the lower working current density of DMFC. Even for the case of deformed GDL in Fig. 8(b), reduction of oxygen concentration from the region under channel to the region under rib is only 2.13%. The concentration polarization due to oxygen transport limit can be neglected. In the other aspect, the ionic potential plays a more important role than the electrical potential in determining the cathode overpotential. In the modeling of a PEMFC, the variation of ionic potential in the cathode CL is very small. The overpotential in the cathode CL can be easily altered by the electrical potential. However, in a DMFC, due to the significant non-uniform distribution of local current density in the anode CL, the variation of ionic potential becomes much larger, which can be seen in Fig. 7(d). This leads to the large variation of ionic potential in the cathode CL through the transport of protons in the PEM, seen in Fig. 8(d). So in the cathode CL of a DMFC, the distribution of overpotential mainly depends on the variation of ionic potential. And the profiles of oxygen concentration and overpotential exhibits the same trends.

Effects of inherent in-plane diffusivity of oxygen on the distribution of oxygen concentration and inherent in-plane conductivity of electrons on the distribution of overpotential in the cathode CL are relatively small, as shown in Fig. 7(b) and (c). And for the case of deformed GDL, it can be seen in Fig. 8(a) that the local current density in the cathode CL shows a much non-uniform distribution along the in-plane direction because of the large variation of

cathode overpotential resulting from the significant change of ionic potential, presented in Fig. 8(d).

3.3. Sensitive analysis of the anisotropic factors of the GDL

The anisotropic factors of the GDL mainly include the inherent anisotropy, deformation, and electrical and thermal contact resistances. In order to investigate the effects of these anisotropic factors individually, the case of anisotropic GDL is picked up to study the effects of inherent anisotropy, including the in-plane permeability and the in-plane electrical conductivity, seen in Sections 3.3.1 and 3.3.2. Then, the deformation effects is analyzed in Section 3.3.3, and electrical and thermal contact resistance effects in Sections 3.3.4 and 3.3.5, respectively.

3.3.1. In-plane permeability

The mass transport in a DMFC is attributed to two mechanisms: diffusion under the gradient of species concentration and convection under the gradient of pressure. According to Darcy's law, it is known that the permeability is an important parameter in the porous media affecting the gradient of the liquid and gas pressure, and consequently the velocities. In the anisotropic GDL, the in-plane permeability is smaller than the through-plane permeability. Fig. 9(a) and (b) shows the effect of in-plane permeability on the liquid velocity in the anode GDL and gas velocity in the cathode GDL. It is seen that the decrease in permeability leads to the decrease in velocities. When the permeability decreases to two orders of magnitude lower than the initial value, the highest liquid velocity in the anode GDL becomes approximately half of the initial velocity; and the highest gas velocity, which is more sensitive to the variation of
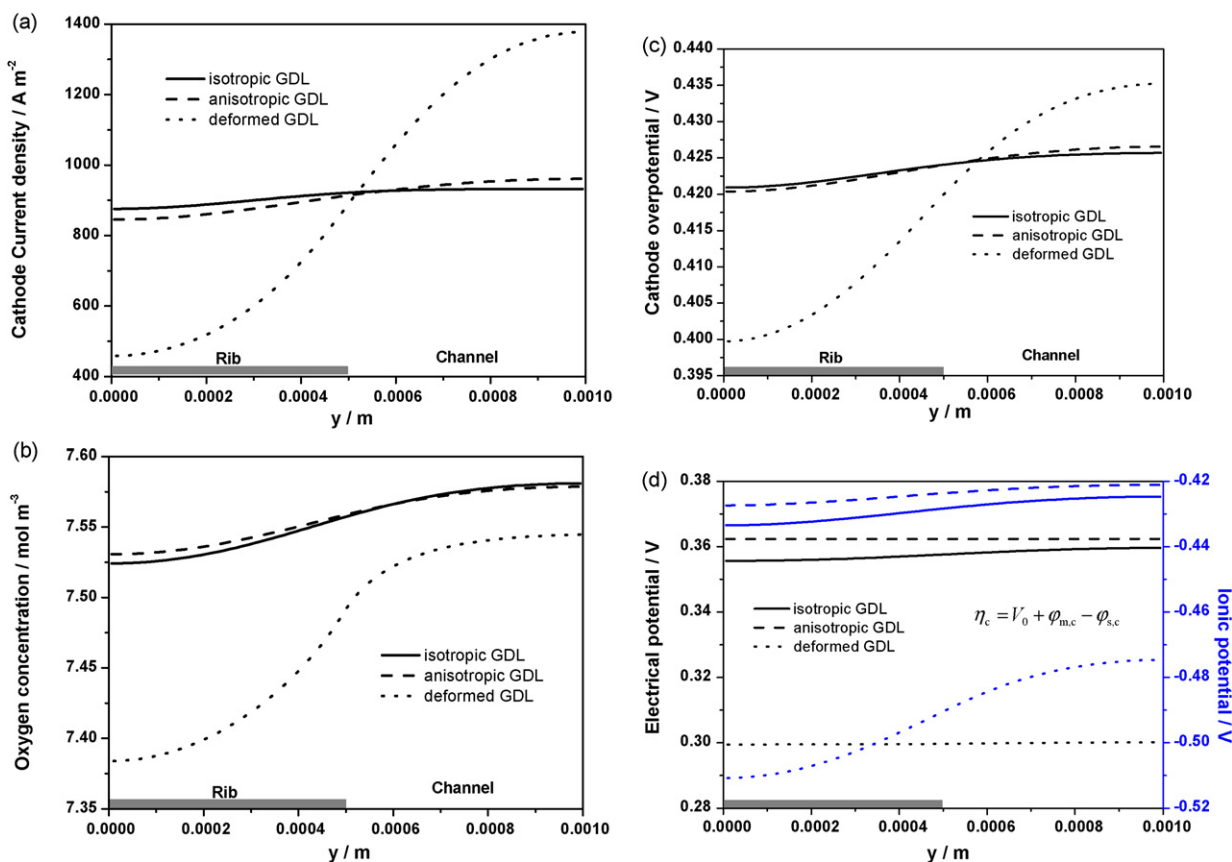
Fig. 8. Distribution of local current density, oxygen concentration, cathode overpotential, and electrical and ionic potential along the in-plane direction in the cathode CL.

permeability, becomes a quarter of the initial value. However, the changes of liquid and gas velocities only give a minor effect on the local current density in the CL, shown in Fig. 9(c). The average current density decreases from 1109.5 A m^{-2} to 1084.7 A m^{-2}, about 2.2% reduction, with the decrease in permeability. These results prove that diffusion mechanism dominate the mass transport in the DMFC. Additionally, Fig. 9(c) also shows that the change of the in-plane permeability mainly affect the current density distribution in the region under rib, so it can be deduced that convection mechanism becomes a little more influential from the region under channel to the region under rib.

3.3.2. In-plane electrical conductivity

As the cathode reactions are more sensitive to overpotential, the profiles of electrical potential and local current density in the cathode CL with different in-plane electrical conductivities are plotted in Fig. 10(a) and (b) to investigate the effects of in-plane electrical conductivity on cell performance. It is shown that the electrical potential becomes smaller and more uniform in the cathode CL with a higher conductivity. These results indicate that it is more easier for electrons to transfer from the rib to the CL under channel. So local reaction rate in this region becomes higher, in view of a higher current density seen in Fig. 10(b). However, the effects of electrical conductivity is much limited. The relative variation is only 2.4% of the current density, from 1082.7 A m^{-2} to 1108.9 A m^{-2}, with a 20-fold increase in the in-plane electrical conductivity. By considering the discussion of effects of anisotropic diffusivities of methanol and oxygen on species transport in Section 3.2, it can be temporally conclude that the inherent anisotropy of the GDL only has a minor effect on the cell performance but has a significant effect on the distribution of physical fields in the membrane electrode assembly (MEA).

3.3.3. Deformation of the GDL

A comparison of the polarization curves of DMFC with different GDL shapes and properties is shown in Fig. 11. It is seen that the polarization curve for the case of isotropic GDL have much little difference from the polarization curve for the case of anisotropic GDL. And this verifies the conclusion in Section 3.3.2. The little larger limiting current density for the case of anisotropic GDL, compared to that of isotropic GDL is primarily attributed to the larger in-plane diffusivities of methanol and oxygen. Also in Fig. 11, the polarization curve for the case of deformed GDL at the anode side shows the lowest limiting cell current density. This is because the inhomogeneous deformation of the anode GDL causes a sharp and inhomogeneous reduction of the porosity of the GDL and consequently a significant decrease in the effective diffusivity of methanol in the anode GDL, as discussed in Section 3.2. Experimental study on the effect of GDL deformation in DMFC is insufficient. However, the polarization curves tested by Ge [4] can support the present numerical results to a certain extend. When the GDL is under a high compression, the performance determined factor in a DMFC is the anode methanol transport, while in a PEMFC, the cathode oxygen transport takes control.

In order to evaluate the effect of deformation of the cathode GDL on cell performance, a comparison of two couples of polarization curves has been conducted: the case of anisotropic GDL versus deformed GDL at the cathode side, and deformed GDL at the anode side versus deformed GDL at both sides. And a very interesting phenomenon is that the deformation of the cathode GDL leads to a little improvement of the cell performance. This phenomenon can be explained by considering the discussion in Section 3.2 that the reactions at the cathode electrode are dominated by cathode overpotential rather than the oxygen concentration. When the cathode GDL is under inhomogeneous deformation, a 93% reduction of the
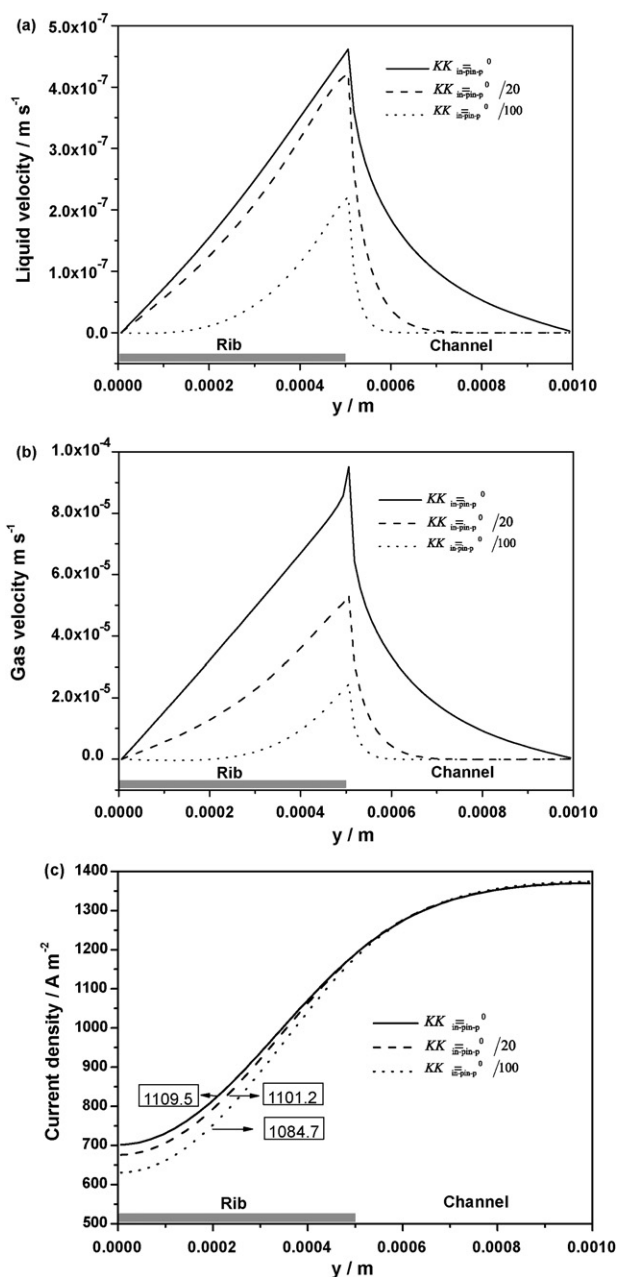
Fig. 9. Effects of in-plane permeability on (a) in-plane liquid velocity in the anode GDL, (b) in-plane gas velocity in the cathode GDL, and (c) current density in the anode CL.

electrical contact resistance at the Rib/GDL interface occurs due to a decrease in the width of GDL under rib from 380 μm to 250 μm. For a certain cell voltage, the decrease in electrical contact resistance leads to the increase in cathode overpotential, and consequently the cell current density becomes higher.

3.3.4. Electrical contact resistance at the GDL/CL interface

Interfacial delamination between the components of fuel cells can be encountered after a long time working, particularly working in a large temperature range [37]. The interfacial delamination between CL and GDL will cause a significant increase in contact resistance. However, it is very hard to experimentally test the value of electrical contact resistance at the GDL/CL interface. Hottinen et al. [8] use the electrical contact resistance at the Rib/GDL interface with a correction considering the volume fraction of Nafion in CL. Nitta et al. [12] use the electrical contact resistance tested from their
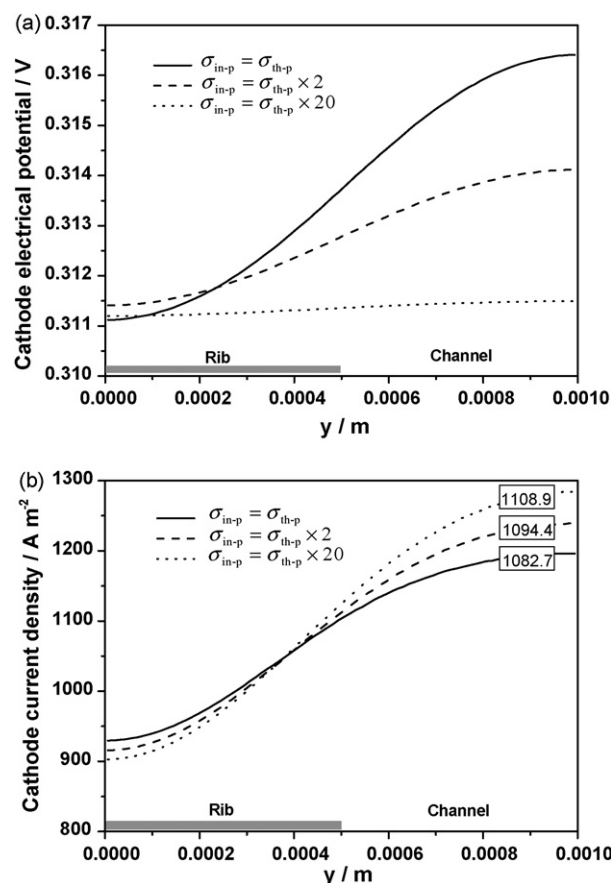

Fig. 10. Effects of in-plane electrical conductivity on the distribution of (a) electrical potential in the cathode CL and (b) local current density in the cathode CL.

experiments [11]. The difference of these two values covers about two orders of magnitude. Based on a prudent attitude, only the electrical contact resistance at the Rib/GDL interface is considered in the base case. And then the effects of the spatial variation of electrical contact resistance at the GDL/CL interface on cell performance are discussed.

Fig. 12(a)–(c) shows the polarization curves of DMFC with different electrical contact resistance at GDL/CL interfaces for the three cases: isotropic GDL, anisotropic GDL and deformed GDL. The similar trends of polarization curves appears in Fig. 12(a) and (b). As the electrical contact resistance becomes lager, a significant
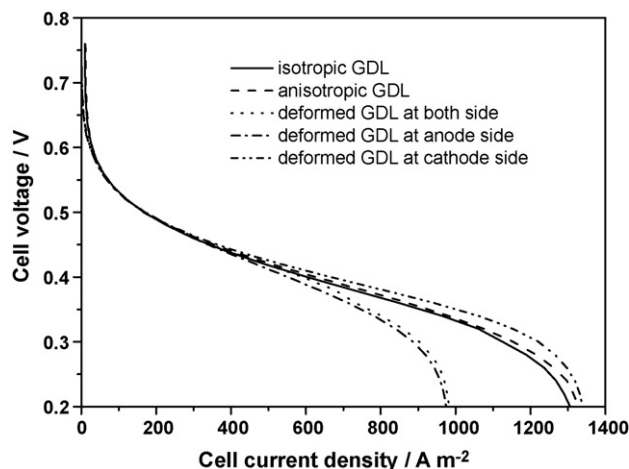

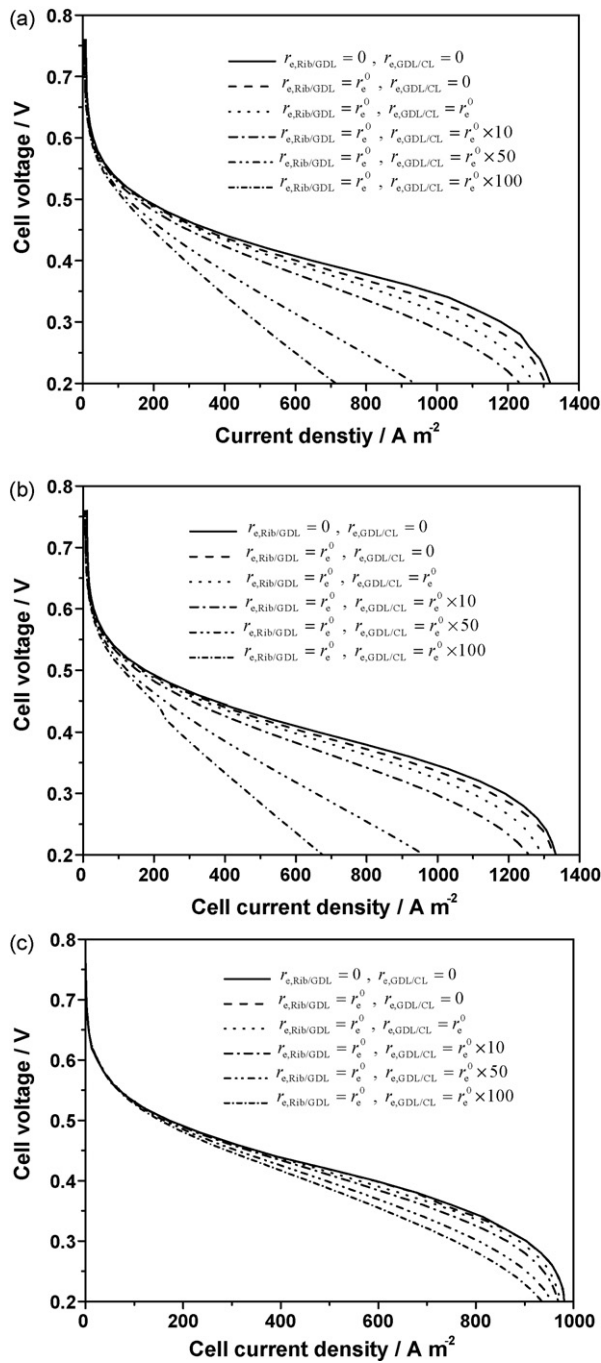Fig. 11. Polarization curves for the DMFCs with different GDL shape and properties.

Fig. 12. Effects of the electrical contact resistance at the GDL/CL interface on cell performance with (a) isotropic GDL, (b) anisotropic GDL, and (c) deformed GDL.
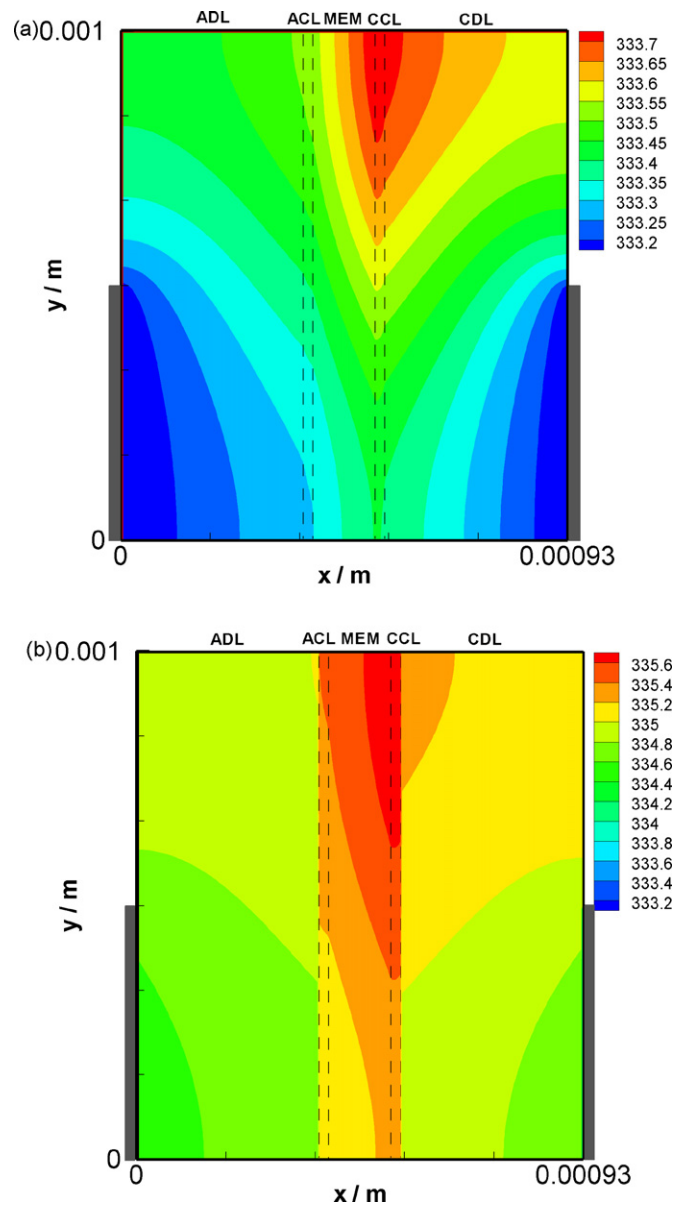

Fig. 13. Comparison of temperature distribution across the MEA with the anisotropic GDL (a) without thermal contact resistance and (b) with thermal contact resistance.

decrease in cell current density is observed in the whole range of cell voltage. At the cell voltage 0.2 V, a decrease in cell current density from 1273.3 A m^{-2} to 714.3 A m^{-2} for the isotropic GDL and from 1294.2 A m^{-2} to 675.7 A m^{-2} for the anisotropic GDL can be seen when the electrical contact resistance at the GDL/CL interface becomes two orders of magnitudes larger. Additionally, the concentration polarization region on the polarization curve disappears when the electrical contact resistance is over ten times larger than the initial value. This is because the species transport in the GDL is sufficient for consumption in the CL at a so small cell current density.

A series of polarization curves for the deformed GDL are shown in Fig. 12(c). The difference of cell current density at a certain cell

voltage in Fig. 12(c) is relatively smaller than those in Fig. 12(a) and (b) because the inhomogeneous deformation of GDLs significantly reduces the electrical contact resistance at both the Rib/GDL and GDL/CL interface. So it can be seen that the effects of electrical contact resistance in the deformed GDL is weakened. In the other hand, it indicates that the numerical model with deformed GDL is more realistic.

3.3.5. Thermal contact resistance at the GDL/CL interface

Thermal management is a key issue in the operation of DMFC. However, the anisotropic parameters of heat transfer are hard to be tested by experiments. The analogy method is used to obtain the heat conductivities from the electrical conductivities in literature [9]. Nitta et al. [10] evaluated the heat conductivities and contact resistance at the Rib/GDL interface by experiments. They found that the deformation of the GDL have a quite small effect on the thermal conductivities. In this work, we also assumed that the thermal conductivities of the GDL is isotropic. However, the thermal contact
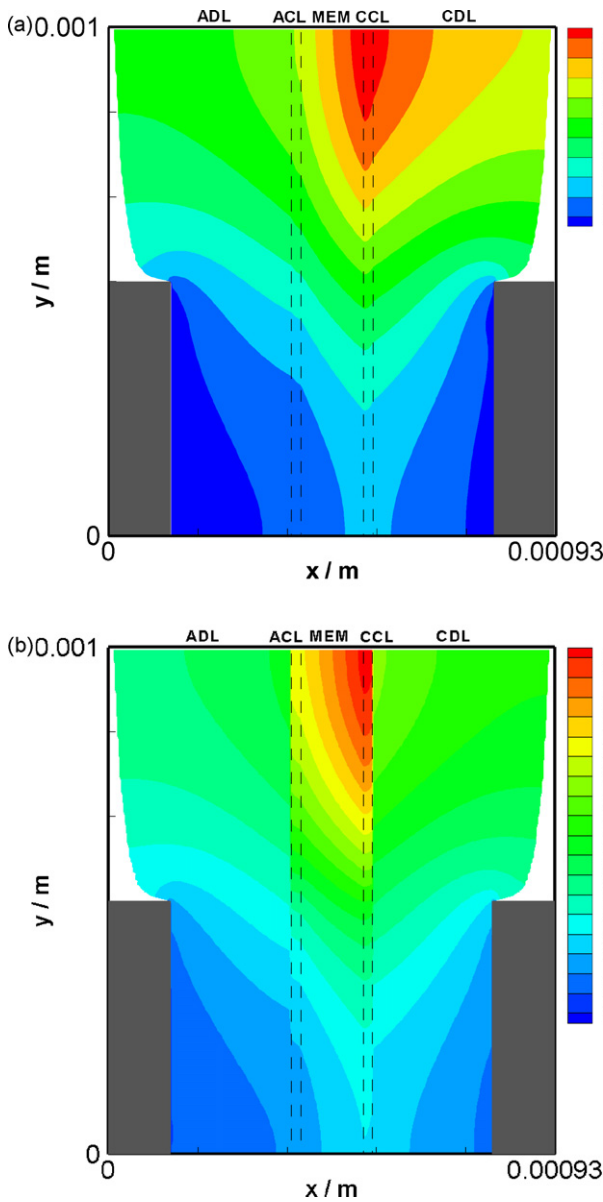
Fig. 14. Comparison of temperature distribution across the MEA with the deformed GDL (a) without thermal contact resistance and (b) with thermal contact resistance.

Fig. 15. Effects of thermal contact resistance at the GDL/CL interface on temperature distribution (a) along the through-plane direction and (b) along the in-plane direction.

resistance at the Rib/GDL interface is affected by GDL deformation. And the thermal contact resistances at both the Rib/GDL and GDL/CL interfaces are assumed to be the same.

The comparisons of temperature distribution across the MEA with and without thermal contact resistance considered are given in Figs. 13 and 14. As the polarization curve for isotropic GDL and anisotropic GDL are so close, and the thermal conductivities in GDLs are assumed to be isotropic, so only the temperature distribution in the MEA with anisotropic GDL is modeled to compare with temperature distribution in the MEA with deformed GDL. It can be seen from Fig. 13 that the highest temperature appears in the region of cathode CL under the channel region because most of heat is generated from the cathode reactions, and the highest local reaction rate occurs in this region. Temperature of the rib is keeping at 333.15 K. And all the heat flux should transfer through the Rib/GDL interface. In Fig. 13(a) the highest temperature is 333.7 K, related to a 0.55 K temperature difference. When thermal contact resistance is considered, the highest temperature becomes 335.6 K, with the temperature difference enlarged to 2.45 K. Besides that, a discontin-
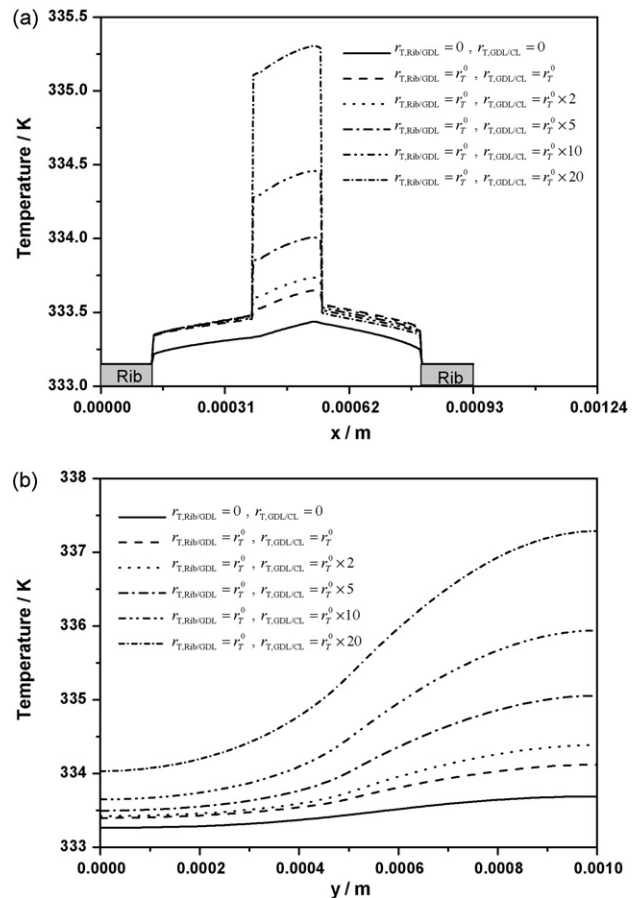
uous temperature jump can be observed at the Rib/GDL and GDL/CL interfaces. The similar temperature distributions are shown in Fig. 14(a) and (b). The temperature difference of the deformed GDL is smaller because of the reduced heat transfer length and, more important, a sharp decrease in thermal contact resistance due to the inhomogeneous deformation. Temperature difference in Fig. 14(b) is only 0.95 K, much smaller than 2.45 K shown in Fig. 13(b).

Similar to the increase in electrical contact resistance at the GDL/CL interface caused by interfacial delamination, the effects of an increase in thermal contact resistance at the GDL/CL interface on temperature distribution in the MEA with deformed GDL are also investigated in this work. The temperature distributions along the through-plane direction at $y = 0.5$ mm and along the in-plane direction in the cathode CL are plotted in Fig. 15(a) and (b), respectively. Fig. 15(a) shows that a higher thermal contact resistance leads to a higher temperature jump at the GDL/CL interface. And the highest temperature difference becomes 4.14 K when the thermal contact resistance increase to 20 times larger than the initial value, seen in Fig. 15(b). The thermal contact resistance hinders the heat release from the MEA to the environment, particularly the region sandwiched by GDLs, including the cathode CL, MEM and anode CL. This has a negative influence on the durability of the fuel cell and could be a vital problem for the operation of fuel cell stack, in which the thermal management becomes more crucial.

4. Conclusions

A two-dimensional two-phase numerical model is developed in this paper to investigate the coupled mass, electrons and heat trans-

port behavior in the DMFC by considering three kinds of anisotropic factors of the GDL, including the inherent anisotropy, the deformation, and thermal and electrical contact resistances. Discussions of the numerical results above indicate that the anisotropy of the GDL has great effects on the transport phenomena in the MEA. Although DMFCs with isotropic GDL and anisotropic GDL give two very close polarization curves, the distributions of species concentration and, particularly, the electrical potential have significant difference. The deformation of the anode GDL plays an important role in determining the cell performance by dominating the diffusive transport of methanol at the anode side. The limiting current density is sharply reduced by the inhomogeneous deformation of the anode GDL. And interestingly, the deformation of the cathode GDL slightly improves the cell performance by significantly reducing the electrical contact resistance in the cathode side. Electrical contact resistance at the Rib/GDL interface, and more importantly, at the GDL/CL interface has a great effect on cell performance. The thermal contact resistance at these two interfaces can significantly enlarge the temperature difference across the MEA. So more efforts are still required to optimize MEA components and assembly technique in order to achieve more even distributed physical field, reduced ohmic resistance, and consequently a better cell performance.

Acknowledgements

References

[1] C.K. Dyer, J. Power Sources 106 (2002) 31–34.
[2] G.J.K. Acres, J. Power Sources 100 (2001) 60–66.
[3] T.H. Zhou, H.T. Liu, J. Power Sources 161 (2006) 444–453.
[4] J. Ge, A. Higier, H. Liu, J. Power Sources 159 (2006) 922–927.
[5] J.G. Pharoah, J. Power Sources 144 (2005) 77–82.
[6] J.G. Pharoah, K. Karan, W. Sun, J. Power Sources 161 (2006) 214–224.
[7] I. Nitta, T. Hottinen, O. Himanen, M. Mikkola, J. Power Sources 171 (2006) 26–36.
[8] T. Hottinen, O. Himanen, S. Karvonen, I. Nitta, J. Power Sources 171 (2007) 113–121.
[9] T. Hottinen, O. Himanen, Electrochem. Commun. 9 (2007) 1047–1052.
[10] I. Nitta, O. Himanen, M. Mikkola, Fuel Cells 8 (2008) 111–119.
[11] I. Nitta, O. Himanen, M. Mikkola, Electrochem. Commun. 10 (2008) 47–51.
[12] I. Nitta, S. Karvonen, O. Himanen, M. Mikkola, Fuel Cells 8 (2008) 410–421.
[13] P. Zhou, C.W. Wu, G.J. Ma, J. Power Sources 163 (2007) 874–881.
[14] P. Zhou, C.W. Wu, J. Power Sources 170 (2007) 93–100.
[15] H. Meng, J. Power Sources 161 (2006) 466–469.
[16] U. Pasaogullari, P.P. Mukherjee, C.Y. Wang, K.S. Chen, J. Electrochem. Soc. 154 (2007) B823–B834.
[17] H. Ju, J. Power Sources 191 (2009) 259–268.
[18] P.C. Sui, N. Djilali, J. Power Sources 161 (2006) 294–300.
[19] W.W. Yang, T.S. Zhao, Y.L. He, J. Power Sources 185 (2008) 765–775.
[20] M. Most, M. Rzepka, U. Stimming, J. Power Sources 191 (2009) 456–464.
[21] G. Murgia, L. Pisani, A.K. Shukla, K. Scott, J. Electrochem. Soc. 150 (2003) A1231–A1245.
[22] J. Divisek, J. Fuhrmann, K. Gartner, R. Jung, J. Electrochem. Soc. 150 (2003) A811–A825.
[23] J.H. Nam, M. Kaviany, Int. J. Heat Mass Transfer 46 (2003) 4595–4611.
[24] M.M. Tomadakis, S.V. Sotirchos, AIChE J. 37 (1991) 74–86.
[25] M.M. Tomadakis, S.V. Sotirchos, AIChE J. 39 (1993) 397–412.
[26] J. Nordlund, G. Lindbergh, J. Electrochem. Soc. 149 (2002) A1107–A1113.
[27] F. Liu, C.-Y. Wang, J. Electrochem. Soc. 154 (2007) B514–B522.
[28] Z. Miao, Y.L. He, X.L. Li, J.Q. Zou, J. Power Sources 185 (2008) 1233–1246.
[29] K. Scott, W. Taama, J. Cruickshank, J. Power Sources 65 (1997) 159–171.
[30] W.W. Yang, T.S. Zhao, Electrochim. Acta 52 (2007) 6125–6140.
[31] S. Um, C.Y. Wang, K.S. Chen, J. Electrochem. Soc. 147 (2000) 4485–4493.
[32] W.W. Yang, T.S. Zhao, J. Power Sources 174 (2007) 136–147.
[33] Z.H. Wang, C.Y. Wang, J. Electrochem. Soc. 150 (2003) A508–A519.
[34] D. Song, Q. Wang, Z. Liu, T. Navessin, M. Eikerling, S. Holdcroft, J. Power Sources 126 (2004) 104–111.
[35] Q. Wang, M. Eikerling, D. Song, Z. Liu, J. Electroanal. Chem. 573 (2004) 61–69.
[36] Y.-L. He, X.-L. Li, Z. Miao, Y.-W. Liu, Appl. Thermal Eng. 29 (2009) 1998–2008.
[37] S. Zhang, X.-Z. Yuan, J.N.C. Hin, H. Wang, K.A. Friedrich, M. Schulze, J. Power Sources 194 (2009) 588–600.